



From Roaming Atoms to Hopping Surfaces: Mapping Out Global Reaction Routes in Photochemistry

Satoshi Maeda,^{*,†} Tetsuya Taketsugu,[†] Koichi Ohno,^{‡,§} and Keiji Morokuma^{*,||}

[†]Department of Chemistry, Faculty of Science, Hokkaido University, Sapporo 060-0810, Japan

[‡]Graduate School of Science, Tohoku University, Sendai 980-8578, Japan

[§]Institute for Quantum Chemical Exploration, Tokyo 108-0022, Japan

^{||}Fukui Institute for Fundamental Chemistry, Kyoto University, Kyoto 606-8103, Japan

S Supporting Information

ABSTRACT: The photodissociation of small molecules occurs upon irradiation by ultraviolet or visible light, and it is a very important chemical process in Earth's atmosphere, in the atmospheres of other planets, and in interstellar media. Photodissociation is an important method used to thoroughly investigate the fundamental issues of chemical reactivity. Photodissociation involves molecules and reaction fragments moving over ground- and excited-state potential surfaces (PESs). Molecules can move on a single PES (adiabatic pathway) or can cross over from one PES to another (nonadiabatic pathways). For a full theoretical understanding of a photodissociation mechanism, all of the important nonadiabatic and adiabatic pathways must be determined. This is not an easy task. We have developed an efficient computational method, called the global reaction route mapping (GRRM) strategy, that allows a theoretical exploration of ground- and excited-state PESs and their crossing seams in an automatic manner. In this Perspective, we summarize our approaches and present examples of their application together with newly determined chemical insights. These include the complex photodissociation mechanism of the formaldehyde molecule, the exclusive excited-state roaming dynamics of the nitrate radical, and all product channels and conformational memory in the photodissociation of the formic acid molecule. Finally, perspectives for the theoretical design of photofunctional molecules are discussed.

■ INTRODUCTION

The photodissociation of small molecules plays important roles in atmospheric processes on the Earth's surface, in the atmospheres of other planets, and in interstellar media. The accurate modeling of these processes is of great significance and requires kinetic data of all possible elementary reactions. Recently, quantum-chemical calculations¹ combined with kinetic theories² have become a powerful means for the prediction of atmospheric reaction rate constants that occur on the ground electronic state potential energy surface (PES).³ However, making similar predictions for photochemical reactions that involve excited electronic state PESs is not that simple for two reasons. One is the accuracy and efficiency of

quantum-chemical calculations on excited electronic states. The other is that it is still difficult to find all of the feasible reaction pathways for high-energy molecules that involve excited electronic states as well as the ground state by a conventional geometry optimization approach. This Perspective presents our approaches to a resolution of the latter problem.

Another motivation for studies of the photodissociation of small molecules is to obtain a thorough understanding of the fundamental issues of these chemical reactions. The photodissociation of small molecules is relatively simple and is ideally suited for this purpose. In particular, the photodissociation dynamics of small molecules has been studied in great detail.⁴ One of the hottest topics in reaction dynamics over the last 10 years is "roaming". This refers to a pathway to molecular products in a unimolecular reaction with a very different configuration space that describes the dissociation to radical products and a subsequent "self-reaction" of the radicals to form molecular products. This unusual pathway was suggested as the most likely of two possible mechanisms to explain a feature in the CO rotational distribution during the photodissociation of H₂CO.⁵ A roaming pathway was found (and named) definitively in 2004 in joint theoretical/experimental work.⁶ Quasiclassical trajectory calculations in ref 6 showed that this unusual pathway is the one that leads to the shoulder feature in the CO rotational distribution described in ref 5. In the trajectories of the roaming pathways, one of the H atoms partially dissociates from H₂CO to form a weakly bound radical–radical (HCO·····H) complex. Instead of dissociation of the complex into two radicals, the partially dissociated H atom roams around the HCO radical and finally abstracts the other H atom from the HCO radical. This results in the formation of the molecular products CO + H₂.⁶ The roaming channel has been discovered in various gas-phase reactions.⁷ Therefore, roaming, which has only been recognized since 2004, is common in gas-phase reactions. The systematic prediction of pathways that follow such an unexpected mechanism is difficult when only a conventional geometry optimization approach is considered, and this is also a topic of this Perspective.

To unravel the entire photoreaction processes, a systematic characterization of the PESs of several excited states as well as the ground state is required. With the Franck–Condon (FC)

Received: December 5, 2014

Published: February 23, 2015



approximation, a photochemical reaction starts at the FC point on an excited-state PES. The system then goes through various reaction pathways depending on the topography of the PESs and the available excess energy. Bond rearrangements or dissociations may occur on the excited-state PES through various transition states (TSs). The system may undergo a nonadiabatic transition to a lower PES and then react on this PES. The system may cascade through several PESs via nonadiabatic transitions.

Nonadiabatic transitions take place efficiently near a seam of the intersection between two PESs.⁸ When the two states have the same spin and space symmetry, the intersection, called a “conical intersection”, spans an $(f - 2)$ -dimensional hypersurface, where f is the number of vibrational degrees of freedom. If the spin multiplicity or the space symmetry is different, two PESs cross in the $(f - 1)$ -dimensional hyperspace, and this is termed the “seam of crossing”. The minimum-energy conical intersection (MECI) and minimum-energy seam of crossing (MESX) represent the lowest-energy structures or the critical points (or, less accurately, the “nonadiabatic transition states”) where nonadiabatic transitions take place efficiently.

To determine all of the possible photochemical reaction pathways for a given system, a systematic search of TSs, MECIs, and MESXs is required for the excited- and ground-state PESs that are accessible at a given photon energy. Figure 1

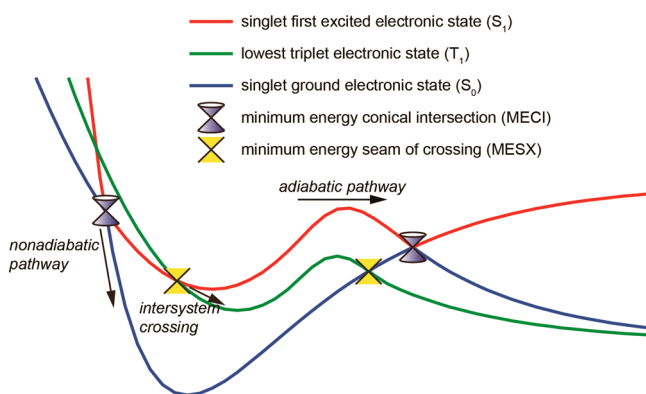


Figure 1. Schematic of the potential energy profiles of the three states S_0 (blue), S_1 (red), and T_1 (green). Cross and cone marks represent the MESX points between the singlet and triplet states and the MECI points between S_0 and S_1 , respectively.

schematically illustrates the potential profiles of a three-state system. Three channels are present for the singlet first excited electronic state S_1 : an adiabatic pathway going over a TS on the S_1 surface, an intersystem crossing (ISC) path to the lower triplet electronic state through the MESX point, and a nonadiabatic pathway leading to the singlet ground electronic state S_0 via the MECI point. These pathways are open when the available photon energy exceeds the energies of the corresponding critical points (i.e., TS, MESX, or MECI). ISC is slow in systems that only contain elements from the upper part of the periodic table because of the small amount of spin–orbit coupling. Transitions to a lower state may take place far from the conical intersection and the seam of the crossing regions by weak vibronic coupling and/or the emission of light, although these processes are generally slower than the three pathways illustrated in Figure 1 when these pathways are open.

Many efficient geometry optimization techniques are available for TSs, MESXs, and MECIs,^{9,10} and these methods

require best-guess structures to initiate the search. It is extremely difficult for chemists to guess where the MECI or MESX is found. Therefore, any optimization method that requires a best-guess structure makes the determination of unexpected crossing structures difficult. A guess-free method is thus required.

Ab initio molecular dynamics (AIMD) simulations are a promising approach to the study of ultrafast photoreaction processes.¹¹ AIMD simulations are highly desirable for studies of ultrafast nonstatistical dynamics. However, this method is extremely expensive and can be executed only for a short period (i.e., for very fast processes) for a limited number of trajectories.

To determine all of the feasible pathways, including those containing slow processes, we have developed automated reaction path search methods^{12,13} that constitute what we have called the global reaction route mapping (GRRM) strategy.¹⁴ These were originally developed for the TSs of the ground-state PES and have been expanded to assist in guess-free searches for the TSs, MECIs, and MESXs of different electronic states. To achieve this, we developed three approaches as briefly explained in the next section.^{15–17} These developments opened the door to the automated exploration of both nonadiabatic and adiabatic reaction pathways for multiple PESs. It should be noted that this approach does not explicitly consider the dynamics as well as the surface-hopping probability. The resulting discussions are thus only qualitative. Nevertheless, it is useful for a qualitative understanding of overviews of complex reaction mechanisms.

In this Perspective, we first describe our GRRM strategy for the systematic exploration of reaction pathways.¹⁴ Here we restrict ourselves to the GRRM strategy for photochemical reactions.^{15–17} With this strategy, we have discovered many unknown and unexpected channels for the photodissociation of small molecules.^{15,18–20} We first applied this method to the photolysis of formaldehyde, H_2CO , which has been extensively studied experimentally and theoretically for decades, and we discovered an unknown nonadiabatic channel that involves the triplet state.¹⁵ A roaming channel on the excited electronic state PES was discovered for the first time during the photolysis of the nitrate radical, NO_3 .¹⁸ Moreover, unlike other roaming channels, no normal (nonroaming) channel coexists, and all of the O_2 was exclusively produced via this excited-state roaming channel. In the photolysis of formic acid, $HCOOH$, the GRRM exploration comprehensively accounted for the numerous different channels observed in various experiments.¹⁹ This result also suggests a mechanism for the conformational memory dynamics observed for the photolysis of the *cis* isomer of formic acid. Other application examples are also briefly introduced.²⁰

METHODS

Seam Model Function (SMF) Approach. The SMF approach is a two-step procedure that allows the exploration and determination of the geometry of the MECI or MESX without a best-guess structure.¹⁵ In the first step, a search for local minima is performed using the following model function $F^{SMF}(Q)$:

$$F^{\text{SMF}}(\mathbf{Q}) = \frac{1}{2}[E^{\text{state-1}}(\mathbf{Q}) + E^{\text{state-2}}(\mathbf{Q})] + \frac{[E^{\text{state-1}}(\mathbf{Q}) - E^{\text{state-2}}(\mathbf{Q})]^2}{\alpha} \quad (1)$$

This function consists of a mean energy term for the two target PESs, $E^{\text{state-1}}(\mathbf{Q})$ and $E^{\text{state-2}}(\mathbf{Q})$, and a penalty function for their energy gap. In eq 1, \mathbf{Q} represents the atomic coordinates $\{Q_i\}$ and α is a constant parameter. Tests have shown that the results are not very sensitive to the value of α , and it is usually set to a standard value of $\alpha = 30$ kJ/mol. We note that similar penalty functions have been used for the geometry optimization of MECIs.^{10e–g} The minimization of $F^{\text{SMF}}(\mathbf{Q})$ reveals a geometry in which both the mean energy and the energy gap are small. This is illustrated in Figure 2a, where the $F^{\text{SMF}}(\mathbf{Q})$ curve shown

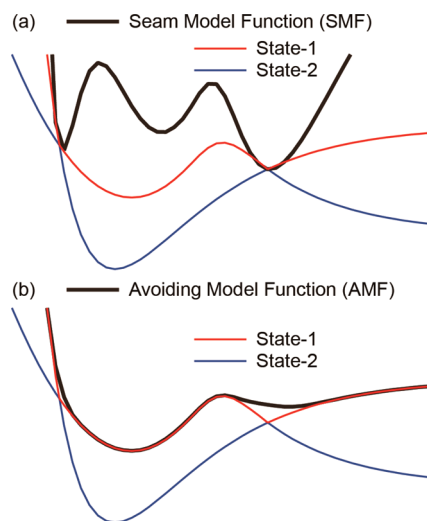


Figure 2. Schematic of (a) the seam model function (SMF) of eq 1 and (b) the avoiding model function (AMF) of eq 2.

with the black thick line has local minima near the two crossing points between the two target states. Therefore, the minima on this function can be used as *approximate* MECI or MESX geometries. Because $F^{\text{SMF}}(\mathbf{Q})$ is a smooth, single-valued function, any automated local-minimum search method can be used without modification. In the second step, the *approximate* geometries obtained in the first step are optimized to the *true* MECI or MESX using any optimization method. The optimization approach in the GRRM code²¹ described below was used in our studies. It should be noted that all of the MESX and MECI structures shown below were fully optimized in the second step and have energy gaps between two target states of less than ~ 0.1 kJ/mol.

Avoiding Model Function (AMF) Approach. The derivatives of the PES calculated by *ab initio* or density functional theory (DFT) methods can be discontinuous at conical intersections. Conical intersections with upper states are generally located in the high-energy regions on the ground-state PES, far from the reaction pathways. However, on the PES of an excited electronic state, conical intersections with a lower electronic state may lie below the important TSs. In some cases, even the lowest-energy point on an excited-state PES is located inside a conical intersection hyperspace. The application of automated reaction path search methods to the PES of excited electronic states is thus not straightforward. Therefore, the following model function was introduced:¹⁶

$$F^{\text{AMF}}(\mathbf{Q}) = \frac{1}{2}[E^{\text{state-1}}(\mathbf{Q}) + E^{\text{state-2}}(\mathbf{Q})] + \frac{1}{2}\sqrt{[E^{\text{state-1}}(\mathbf{Q}) - E^{\text{state-2}}(\mathbf{Q})]^2 + 4U(\mathbf{Q})^2} \quad (2)$$

in which the coupling term $U(\mathbf{Q})$ is given by

$$U(\mathbf{Q}) = \frac{\beta}{2} \exp\left[-\left(\frac{E^{\text{state-1}}(\mathbf{Q}) - E^{\text{state-2}}(\mathbf{Q})}{\beta}\right)^2\right]$$

where \mathbf{Q} denotes the atomic coordinates $\{Q_i\}$, $E^{\text{state-1}}(\mathbf{Q})$ is an adiabatic PES of the target (upper) state, $E^{\text{state-2}}(\mathbf{Q})$ is an adiabatic PES of the lower state, and β is a constant parameter. This expression for F^{AMF} is similar to the well-known equation used for the diabatic/adiabatic transformation of two-state systems, where $E^{\text{state-}n}$ are diabatic PESs. For F^{AMF} , in contrast, $E^{\text{state-}n}$ are adiabatic PESs. The model coupling term $U(\mathbf{Q})$ modifies the conical intersection regions. This is illustrated in Figure 2b. The $F^{\text{AMF}}(\mathbf{Q})$ curve shown by the black thick line is smooth around the two crossing points. Any automated reaction path search method that has been developed for smooth PESs can thus be applied to F^{AMF} . The function $U(\mathbf{Q})$ is designed so that it has an effect only in limited regions with a small energy gap. Hence, F^{AMF} is very similar to the PES $E^{\text{state-1}}$ in areas with a large energy gap, as illustrated in Figure 2b. The accuracy (i.e., how well stationary structures on F^{AMF} reproduce those on $E^{\text{state-1}}$) depends on the β value. In our experience, β should be set to $\sim 1/10$ the vertical excitation energy. In the discussed examples, β was set to 30 kJ/mol.

The local-minimum and TS structures on the excited-state (adiabatic) PES $E^{\text{state-1}}$ can be explored in two steps: (1) an exploration of the *approximate* local-minimum and TS structures as local minima and first-order saddle points, respectively, on F^{AMF} by any automated reaction path search method and (2) the reoptimization of the *true* local-minimum and TS structures on the PES $E^{\text{state-1}}$ using the *approximate* structures as initial guesses. It should be noted that all of the local-minimum and TS structures discussed in this paper are fully optimized *true* structures on adiabatic PESs.

Branching Plane Updating (BPU) Approach. On a conical intersection, there are two directions that lift the degeneracy of the two adiabatic PESs: the gradient difference vector (GDV) direction and the derivative coupling vector (DCV) direction. The plane defined by these two vectors is called the branching plane (BP), and the BP is required at every MECI optimization step to retain the geometry on the conical intersection hyperspace. The GDV is the difference between the gradient vectors of the two target states and can be readily calculated. The DCV, however, requires extra calculations. Furthermore, the DCV is not available in all *ab initio* theories. We thus developed an approach to estimate the BP without calculation of the DCV, using a history of the optimization steps.¹⁷

We express a BP at the k th optimization step by two vectors, \mathbf{x}_k and \mathbf{y}_k , where \mathbf{x}_k is a unit vector parallel to the GDV for the adiabatic energy at the k th step and \mathbf{y}_k is a unit vector on the BP perpendicular to \mathbf{x}_k . At the k th step, \mathbf{x}_{k-1} , \mathbf{y}_{k-1} , and \mathbf{x}_k are known and \mathbf{y}_k is unknown. In the first-order approximation of diabatic PESs, the BP (i.e., the xy plane) does not change by any geometrical displacement. In other words, the first-order BP at the k th step is simply the plane defined by \mathbf{x}_{k-1} and \mathbf{y}_{k-1} . At the k th step, \mathbf{x}_k is calculated exactly and may have a component not

contained in \mathbf{x}_{k-1} or \mathbf{y}_{k-1} because of the higher-order terms obtained when determining \mathbf{x}_k . \mathbf{y}_k can then be estimated from the unchanged first-order BP, and such a \mathbf{y}_k should be written as a linear combination of \mathbf{x}_{k-1} and \mathbf{y}_{k-1} as follows: $\mathbf{y}_k = s\mathbf{x}_{k-1} + t\mathbf{y}_{k-1}$. Because \mathbf{y}_k is a unit vector orthogonal to \mathbf{x}_k , we obtain the following simultaneous equations for s and t :

$$\begin{aligned} s(\mathbf{x}_{k-1} \cdot \mathbf{x}_k) + t(\mathbf{y}_{k-1} \cdot \mathbf{x}_k) &= 0 \\ s^2 + t^2 &= 1 \end{aligned} \quad (3)$$

By solving eq 3, we obtain \mathbf{y}_k as

$$\mathbf{y}_k = \frac{(\mathbf{y}_{k-1} \cdot \mathbf{x}_k)\mathbf{x}_{k-1} - (\mathbf{x}_{k-1} \cdot \mathbf{x}_k)\mathbf{y}_{k-1}}{\sqrt{(\mathbf{y}_{k-1} \cdot \mathbf{x}_k)^2 + (\mathbf{x}_{k-1} \cdot \mathbf{x}_k)^2}} \quad (4)$$

This \mathbf{y}_k is used together with \mathbf{x}_k to construct an updated BP at the k th step, and they are saved for the next step. At the initial step, the first-order BP (\mathbf{x} and \mathbf{y} from the last step) is not available. A plane made of \mathbf{x}_0 and the mean energy gradient vector was used as an initial BP. This BP is exact at the stationary points in the conical intersections because the mean energy gradient vector does not contain any components perpendicular to the BP at these points. The DCV is thus no longer necessary at every optimization step when this BPU algorithm is employed. Although this scheme in part assumes a first-order approximation, higher-order effects are taken into account by using the exact \mathbf{x}_k , and this works very well as demonstrated in numerical tests.¹⁷

Structure Exploration and Optimization. With the above approaches, our own automated reaction path search methods were applied for the exploration of stationary structures: local minima and TSs on the ground- and excited-state PESs as well as MECIs and MESXs between adjacent PESs. We have developed two automated reaction path search methods. In this study, the anharmonic downward distortion following¹² (ADDF) method was mainly employed. Along a typical reactive potential curve, an anharmonic downward distortion (ADD) arises and increases toward a TS. Therefore, TSs and local minima beyond the TSs can be found by following the ADDs starting from a local minimum. The application of this ADDF procedure to all of the obtained local minima provides a full reaction path network including local minima and TSs on a given PES. The other automated reaction path search method called the artificial force induced reaction¹³ (AFIR) method. In the AFIR method, two (or more) fragments are pushed together by minimizing the AFIR function, which is composed of the adiabatic potential energy and an artificial force term. The minimization path of the AFIR function (the AFIR path) can be an *approximate* reaction path. A TS and a product for the corresponding reaction can be obtained from the AFIR path. A sufficient ensemble of the AFIR path and the resulting reaction path network can be obtained by the multicomponent algorithm^{13c} (MC-AFIR) for bimolecular and multicomponent reactions and by the single-component algorithm^{13d} (SC-AFIR) for intramolecular reactions. In the photochemical GRRM strategy, the ADDF and AFIR methods, which have previously been applied mainly to the ground-state PES, are applied to F^{SMF} and F^{AMF} .

As discussed above, the application of ADDF and AFIR to F^{SMF} and F^{AMF} generates *approximate* stationary structures. These approximate structures can then be reoptimized by any standard geometry optimization method. We used a quasi-Newton method known as rational function optimization

(RFO),²² implemented in the GRRM code,²¹ for local-minimum and TS geometry optimizations. In MESX and MECI optimizations, the gradient projection (GP) method was used. In the GP method,^{10c,h} a gradient vector is recomposed as the sum of two vectors: the difference gradient between the two PESs and the projected mean-energy gradient for the two PESs. The projected mean-energy gradient is a mean-energy gradient multiplied by the projection matrix that eliminates the gradient components of degeneracy-lifting directions, i.e., the GDV direction in MESX optimization and the GDV and DCV directions in MECI optimization. An optimization using the recomposed gradient of the GP method thus minimizes the energy gap in these GDV or GDV and DCV directions and the mean energy on the remaining $(3N - 7)$ - or $(3N - 8)$ -dimensional hypersurface. In this study, MESX and MECI optimizations were also performed with the RFO method using the recomposed gradient of the GP method.¹⁷

Refining Structures and Energies toward Reliable Prediction. A third step is also required. Usually, the above-mentioned automated exploration is performed by a computationally less demanding method such as CASSCF with a small active space and basis set. All of the obtained structures are fully reoptimized at a more reliable computational level such as CASPT2 with a large active space and basis set. However, in the excited-state calculations, the dependence of the topography of the PES on the computational level is relatively large. Therefore, we sometimes face serious cases wherein the paths obtained from low-level automated searches disappear during the final high-level reoptimization process. In these cases, we locate the corresponding path manually using double-ended-type reaction path search methods such as the double-end version of the ADDF method and the locally updated plane method.^{23,24} We note that this manual step is the most difficult part for people who conduct these studies. As will be shown in the following examples, the automated search sometimes only provides hints about the unknown and unexpected reaction mechanisms, and a careful examination of the search output is often critically important to determine the real mechanisms.

Summary of the Workflow. The workflow can be summarized as follows:

- Application of the ADDF method to the PESs for all of the relevant electronic states to find the local-minimum and TS structures, where the AMF approach is employed in electronic excited state applications.
- Application of the ADDF-SMF approach to all adjacent PES pairs to find the MESX and MECI structures for the two PESs.
- Reoptimization of each critical point in stages (A) and (B) (obtained with a computationally less demanding method such as CASSCF) using a more reliable computational method such as CASPT2.

Computational Program. All of the above-mentioned approaches (i.e., SMF, AMF, BPU, ADDF, and AFIR) have been incorporated into the GRRM program and are available in the latest version (GRRM14).²¹ The GRRM program calls an electronic structure calculation code as an external subroutine to obtain the energy, gradient, and Hessian of the target electronic state(s) at a given geometry. Using these PES data, the GRRM program modifies the molecular geometry. In the following applications, the MOLPRO²⁵ program was called to obtain the PES data using multireference CASSCF and CASPT2 theories. DFT calculations for the ground-state PES

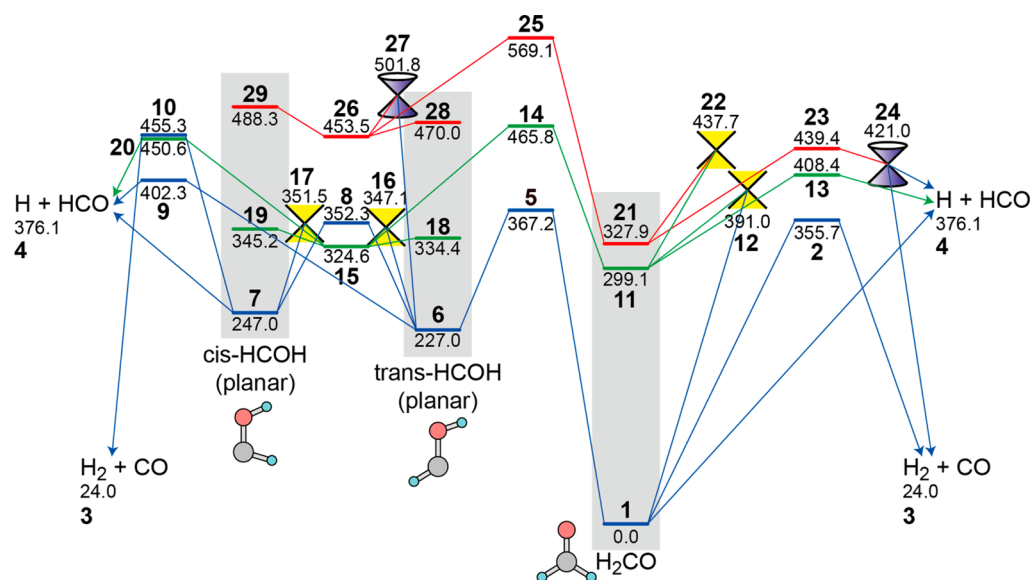
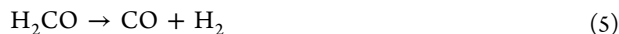


Figure 3. Potential energy profiles (in kJ/mol) for the three states S_0 (blue), S_1 (red), and T_1 (green) of H_2CO at the CASPT2 level. Cross and cone marks represent MESX points for the singlet and triplet states and the MECI points for S_0 and S_1 , respectively.

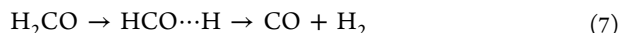
and spin-flip time-dependent DFT (TDDFT) calculations for MECI optimizations were performed using Gaussian 09²⁶ and GAMESS,²⁷ respectively, in combination with the GRRM program. In GRRM14, tight connectors (i.e., internally implemented interfaces) to these three quantum-chemical calculation programs are available. Furthermore, any quantum-chemical or molecular-mechanics program can be used with the GRRM code by a loose connector developed by the users.

RESULTS

Formaldehyde Molecule: Complex Photodissociation Mechanisms for a Simple Molecule. The first example is the photolysis of formaldehyde at relatively low photon energies (<383 kJ/mol). It was suggested experimentally that photodissociation occurs on the PES of the singlet ground electronic state (S_0) after internal conversion (IC) from the singlet first excited electronic state (S_1).²⁸ The dynamics and reaction pathways on the S_0 PES have been studied extensively.²⁹ Early studies focused on the following two channels:



For the channel shown in eq 5, the corresponding TS was determined computationally for the first time in 1974.^{29b} The radical dissociation channel (eq 6) can occur both from the S_0 state and from the lowest triplet electronic state (T_1), and therefore, the T_1 PES has also been studied.³⁰ Additionally, a third channel, called “roaming”, also exists and was discovered in 2004.⁶ The third channel can be expressed as follows:



where one of the H atoms, once partially dissociated, roams around the HCO fragment and finally abstracts the other H atom to generate $CO + H_2$. The dynamics of the partially dissociated H atom has been termed “roaming”. The remaining question concerning the low-energy photolysis was how the excited molecules reach the S_0 PES from the S_1 PES. However,

knowledge about the nonadiabatic pathways has been scarce until recently.³¹ Therefore, we performed an SMF/ADDF search for the MECI and MESX structures.¹⁵

Figure 3 shows a potential energy profile for the three low-lying states S_0 , S_1 , and T_1 of H_2CO . These calculations were performed at the CASPT2/aug-cc-pVDZ level with the full-valence active space (MS-CASPT2 for S_0 and S_1 and SS-CASPT2 for T_1). To avoid the intruder state problem of CASPT2, a shift parameter of 0.3 was applied. In this figure, for clarity, we do not show the PES areas of the very high energy structures such as the $H_2O \cdots C$ and related pathways as well as the pathways for the roaming channels. The molecular channel occurs through TS 2, which lies 355.7 kJ/mol above the ground state of H_2CO . At 376.1 kJ/mol, the radical dissociation channel to $H + HCO$ opens. At higher than 408.4 kJ/mol, the radical channel is also apparent from the T_1 PES through TS 13. These energetics correspond well with the available experimentally determined energy thresholds.

ISC from T_1 to S_0 was initially considered to occur in the potential well of the H_2CO form. However, in 2008, low-energy T_1/S_0 MESXs 16 and 17 were located in the potential well of hydroxycarbene in the HCOH form, and ISC was proposed to take place from this HCOH form.³² To visit the potential well of HCOH on the T_1 PES, the high-energy TS 14 for the 1,2-shift of the H atom must be overcome, and this was suggested to take place by quantum tunneling. In 2009 we explored the MESX and MECI points that involve the S_0 , S_1 , and T_1 PESs systematically by the SMF/ADDF approach. We discovered the new MESX point 12 between the S_0 and T_1 PESs.¹⁵

Adopting our MESX 12, we proposed a new mechanism for low-energy photolysis as follows. After the photoexcitation, the system stays around the S_1 local minimum 21 for a long time because all of the structures connected to 21 are high in energy. The S_1/T_1 ISC takes place by trickling down from S_1 to T_1 for all of the geometries, while the molecule in the S_1 state spends a long time oscillating around 21. This occurs because the PESs for the S_1 and T_1 states have similar energies throughout the basin of 21. Although the probability at each geometry may be small because the spin–orbit coupling between the two states S_1 and T_1 that belong to the same ($n \rightarrow \pi^*$) electronic

configuration is small, the integrated probability over a long time could be substantial. Once the system comes down to T_1 from the S_1 basin region, the T_1/S_0 ISC through the newly found MESX point 12 (391 kJ/mol) takes place within the H_2CO basin. This mechanism based on CASPT2 energetics is consistent with the result obtained by highly accurate MRCISD(Q)/aug-cc-pV5Z calculations.³³ After the transition to S_0 , the dynamics on the S_0 PES should start in the potential well of H_2CO .

Our mechanism was confirmed by three-state trajectory surface hopping (3S-TSH) simulations involving the S_0 , S_1 , and T_1 states.³⁴ In the 3S-TSH simulations, highly accurate (analytically fitted) PESs were used, and hopping between PESs was treated with Tully's fewest switches algorithm. The 3S-TSH simulations demonstrated that the above-mentioned decay mechanism involving the S_1/T_1 trickling down and the subsequent T_1/S_0 ISC near 12 is the major process. Furthermore, a new unexpected dynamics was discovered in which the system decays to the S_0 PES and then isomerizes to HCOH on the S_0 PES before dissociation. In these trajectories, the system hopped up to the T_1 PES and then hopped down to the S_0 PES near 16 and 17. This is energetically allowed, as shown in Figure 3.

When the available energy is higher than the T_1 barrier 13 (and lower than 23), the H atom dissociation mainly takes place on the T_1 PES. This was confirmed by the sudden decrease in the HCO product's rotational energy around the energy of 13.^{30b} This is strong evidence of the involvement of the T_1 PES in the decay mechanism during low-photon-energy photolysis. If the available energy is higher than the S_1 TS 23, H atom dissociation can take place on the S_1 PES. MECI 24 is present after H atom dissociation,³⁵ and the system can also reach the S_0 PES via this MECI. A symmetric CI structure that corresponds to a saddle point within the same CI is also known.^{31b} CASSCF on-the-fly dynamics studies have shown that a nonadiabatic transition takes place at MECI 24 after H atom dissociation through 23, and these dynamics result in the generation of the molecular products CO + H_2 by a recombination between H and HCO.³⁶ This path may be an alternative (fourth) channel that may open when the available energy is relatively high (higher than ~440 kJ/mol).

Some discussion has occurred about the TS of the roaming channel (eq 7).^{6,37–39} It was first suggested that no explicit TS exists for this channel.⁶ However, three different TSs that may be relevant to this channel have been reported: (1) a TS that connects 1 with 3 directly and has a structure in which the roaming H atom is in the out-of-plane direction of the HCO fragment;^{37,39} (2) a TS that connects 1 and 7 directly and has a structure in which the roaming H atom is in the out-of-plane direction of the HCO fragment;^{12b} and (3) planar TSs for a multistep roaming path in which the roaming H atom migrates once to the O atom side of the HCO fragment and then goes back and abstracts the other H atom.³⁸ Although the relevance of the second path to the roaming channel has not been discussed,^{12b} we reconsidered it because the atomic movements in this path also involve long-distance H atom migration.

Figure 4 shows a reaction path network for the long-distance H atom migration around HCO. Although these pathways have previously been reported at different computational levels, for consistency we recalculated them at the CASPT2 level, and all three paths were found and confirmed by the computational level used. In all of the TSs in Figure 4, the H atom goes through regions 3.5–4.0 Å from the HCO fragment. These TSs

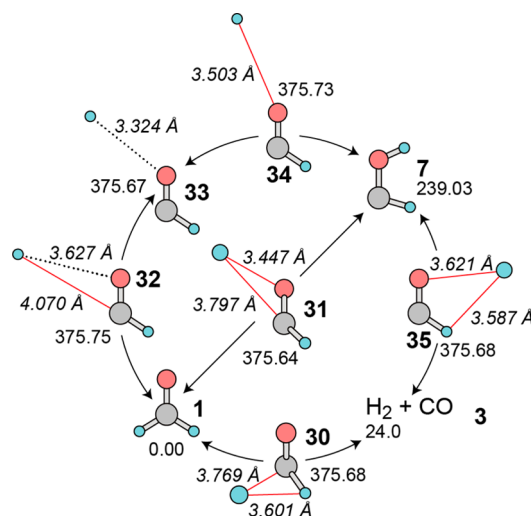


Figure 4. Reaction path network for the roaming channels of H_2CO at the CASPT2 level. Energy values (in kJ/mol) are shown near the corresponding structures. Some important bond lengths are shown in italics. Arrows are shown from TSs 30, 31, 32, 34, and 35 toward the local minima 1, 7, and 33 and the dissociated product 3. Bonds that rearrange at each TS are shown with red lines, and weak coordination bonds are shown with dotted lines.

lie only slightly below the potential asymptote of the $H + HCO$ direct dissociation channel at 376.1 kJ/mol. This is typical in the many roaming channels discovered to date.⁷ However, it is difficult to tell which path is the most important using only the potential profile. Roaming trajectories that go through various HCO fragment directions have been discovered in extensive molecular dynamics simulations.⁶ Moreover, the potential valleys for these roaming paths are very shallow, and their trajectories can easily deviate from the corresponding minimum-energy paths. From this viewpoint, the initial suggestion of the absence of an explicit TS for this channel would be partially correct. Nevertheless, in general roaming channels can be represented by some TSs, and by locating them one can discuss the existence of roaming channels.⁴⁰ For quantitative discussions, it is obvious that more reliable analyses such as extensive molecular dynamics simulations⁴¹ and/or extended transition state theory and phase space theory simulations^{42,43} are required. Moreover, one needs to choose the computational level carefully because the roaming pathways pass near a dissociation limit ($H + HCO$ in this case) and the shapes of the PESs in such asymptote regions can easily change depending on the computational level.

Nitrate Radical: Exclusive Excited-State Roaming Mechanism. Roaming channels are known to occur on the ground electronic state and as a minor channel. However, questions arise about the possibility of exclusive roaming and whether roaming on the electronic excited state is possible. The discovery of such a case would considerably expand the generality and the importance of the roaming channel.

In 2011, for the photolysis of NO_3 , we discovered an exclusive excited-state roaming channel, which breaks both of these two known rules.¹⁸ The photodissociation dynamics of NO_3 has been studied extensively, mainly because of its relevance in atmospheric chemistry.⁴⁴ It has two channels:



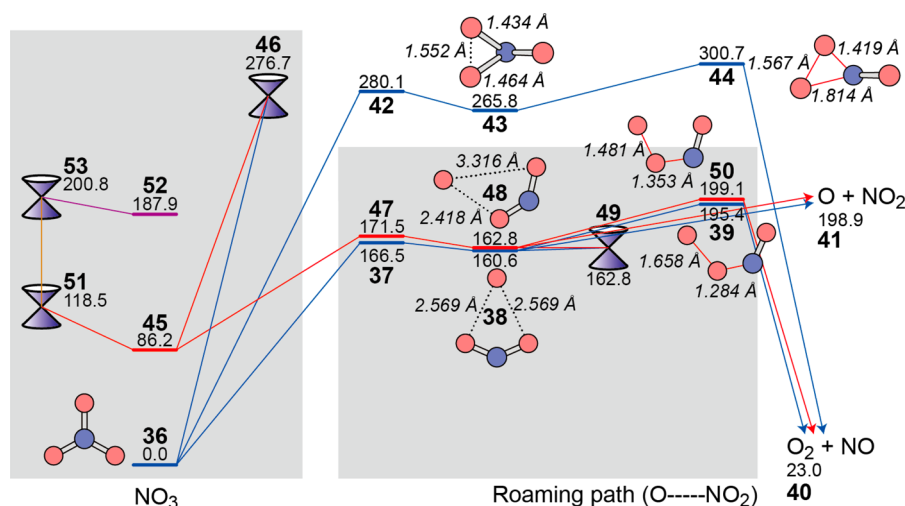


Figure 5. Potential energy profiles (in kJ/mol) of the four states D_0 (blue), D_1 (red), D_2 (orange), and D_3 (purple) of NO_3 at the CASPT2 (for D_{0-2}) or CASSCF (for D_3) level. Cone marks represent MECI points between two doublet states.

The path shown in eq 8 is observed only over a very narrow wavelength range of 585–595 nm (204.5–201.1 kJ/mol), and that in eq 9 is predominant at wavelengths less than 585 nm. However, no theoretical reaction path that explains the $\text{NO} + \text{O}_2$ channel at 585–595 nm was known until 2011. In 2010 it was shown experimentally that at 588 nm (203.4 kJ/mol) there are two pathways that give vibrationally hot and cold O_2 molecules, respectively.⁴⁵ A roaming path was suggested to be responsible for the generation of vibrationally hot O_2 because roaming channels have previously been shown to generate vibrationally hot products as a result of the nearly barrierless recombination of two unstable fragments.⁷ No clear interpretation existed for the vibrationally cold product. We thus conducted SMF/ADDF and AMF/ADDF searches and discovered a highly unexpected mechanism, as discussed below.

Figure 5 shows potential energy profiles for the four states D_{0-3} of NO_3 . The profiles were obtained by MS-CASPT2/6-31+G* for D_{0-2} and four-state-averaged CASSCF/6-31+G* calculations for D_3 with the 11 electron, eight orbital (11e, 8o) active space.¹⁸ To avoid the intruder state problem of CASPT2, a shift parameter of 0.3 was applied. For clarity, only the important stationary points that are discussed below are shown in Figure 5. At the FC point with D_{3h} symmetry, the degenerate D_1 and D_2 states are dark states and the degenerate D_3 and D_4 states are bright states. The 588 nm photon excites NO_3 to D_3/D_4 , and the dynamics start from D_3 and D_4 . The molecules excited to D_4 can easily move to D_3 as the system is already in the intersection hyperspace at the FC point. MECI 53 between D_3 and D_2 is close to the FC point, and the system rapidly decreases to D_2 . The lowest-energy point on the D_2 PES is located inside the D_1/D_2 conical intersection as MECI 51. The system thus moves to D_1 . On the D_1 PES, there is no pathway that further decays to the D_0 PES because the lowest MECI 46 is very high in energy and is difficult to reach with the available energy. The dissociation dynamics thus starts from D_1 minimum 45 rather than D_0 minimum 36.

N–O bond dissociation occurs on the D_1 PES through TS 47. However, the dissociating O atom stays around the NO_2 fragment and forms a weak $\text{NO}_2 \cdots \text{O}$ complex 48 on D_1 . In the $\text{NO}_2 \cdots \text{O}$ form, the system can move to D_0 through MECI 49. Finally, an intramolecular recombination between NO_2 and O takes place either on the D_1 PES through TS 50 or on the D_0

PES via TS 39. These pathways exhibit roaming O atom dynamics. Interestingly, the roaming dynamics involve not only the ground electronic state D_0 but also the first excited state D_1 , in contrast to the previously reported roaming channels. Furthermore, the next-lowest TS generates the same products, i.e., $36 \rightarrow 42 \rightarrow 43 \rightarrow 44 \rightarrow 40$, which is not accessible with a photon energy of 588 nm. This suggests that the $\text{NO} + \text{O}_2$ products are exclusively generated from roaming dynamics starting at the excited electronic state D_1 . The discovery of this exclusive roaming channel starting from an excited electronic state breaks two known conditions of roaming: on the ground electronic state and in small fraction. This extends the significance of roaming significantly in photochemical reaction dynamics.

Our proposal was confirmed three ways. First, DFT-based on-the-fly dynamics simulations were performed, starting from the recombination TSs 39 and 50.¹⁸ The trajectory from the higher TS 50 on the D_1 PES gave vibrationally cold O_2 , whereas vibrationally hot O_2 was produced by the trajectory from the lower TS 39 on the D_0 PES. These trajectories explain the generation of vibrationally cold and hot O_2 as minor and major products, respectively, in the earlier experiments.⁴⁵ Second, the NO Λ doublet propensity (correlation between the NO rotational plane and the direction of the unpaired electron) was determined by an ion-imaging experiment.⁴⁶ In the recombination TSs 50 and 39, the unpaired electron is directed toward the out-of-plane direction in 50 and toward the molecular plane in 39. Therefore, the determination of the Λ doublet propensity is strong evidence for the involvement of these two recombination TSs. Third, extensive dynamics simulations were performed using the global PESs⁴⁷ obtained by fitting analytical potential functions to the 90 000 MS-(17e, 13o)-CASPT2/aug-cc-pVTZ energies for D_0 and D_1 .⁴⁸ These molecular dynamics simulations starting from either 36 or 45 only gave the products $\text{NO} + \text{O}_2$ with a roaming mechanism, and they quantitatively reproduced the experimental vibrational and rotation distributions of the products. However, the simulations did not consider the nonadiabatic transition between D_0 and D_1 .⁴⁸ The branching ratio of the $\text{NO} + \text{O}_2$ products is not known from the simulations or from any other work. Future quantitative simulations that account for the

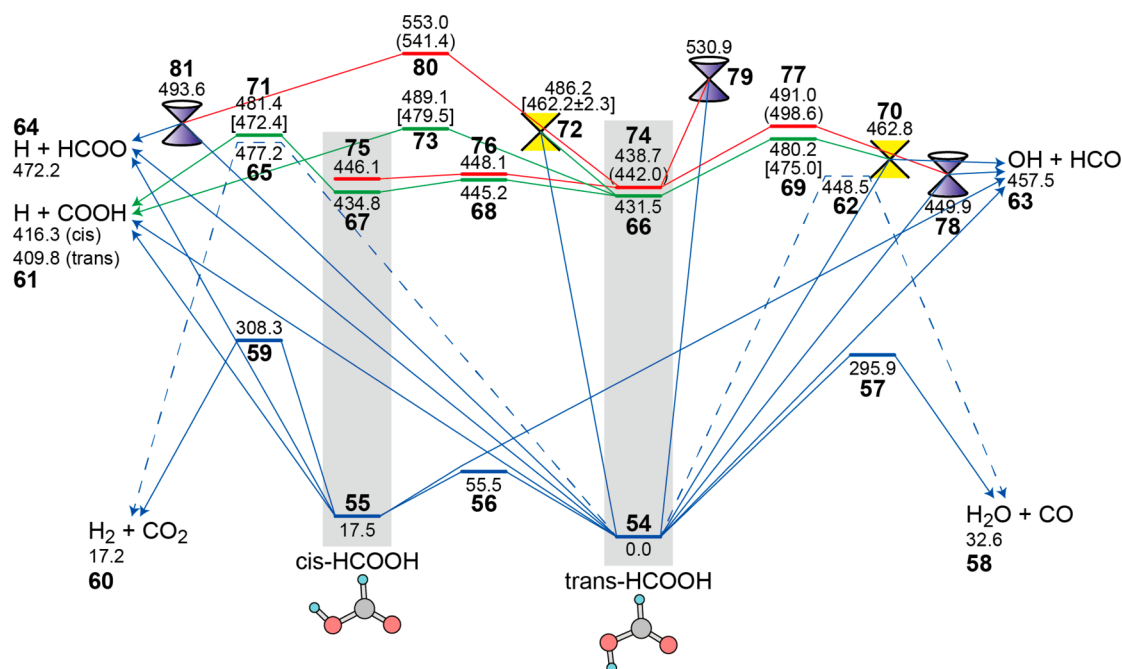


Figure 6. Potential energy profiles (in kJ/mol) for the three states S_0 (blue), S_1 (red), and T_1 (green) of HCOOH at the CASPT2 level. Cross and cone marks represent MESX points between the singlet and triplet states and MECI points between the two singlet states, respectively. Energies at the MRCISD(Q)//CASPT2 and UCCSD(T)//UCCSD levels are shown in parentheses and square brackets, respectively, for selected structures in a quantitative comparison with the available experimental data. The uncertainty of ± 2.3 kJ/mol at MESX 72 indicates a S_0/T_1 energy gap of 4.6 kJ/mol at the UCCSD(T) level calculated for the UCCSD-optimized MESX geometry. The roaming channels that involve the partially dissociated TSs 62 and 65 in the form of $\text{HCO}\cdots\text{OH}$ and $\text{HCOO}\cdots\text{H}$, respectively, are shown with dashed lines.

nonadiabatic coupling of adiabatic potentials are required for a further understanding of this system.⁴⁹

Formic Acid Molecule: All Product Channels and Conformational Memory. The third example is the photodissociation of the trans and cis isomers of the formic acid molecule, HCOOH. The photolysis of *trans*-HCOOH has been a target of many experimental and theoretical studies.⁵⁰ However, the cis isomer, which easily undergoes isomerization to the lower-energy trans isomer, has been studied only in an Ar matrix.⁵¹ For *trans*-HCOOH, the following five channels have been observed.



In this section, we will show how the results of a systematic reaction pathway search can be used to assign pathways for all of the experimental reaction channels. The special topic discussed is the conformation-specific dynamics observed for *cis*-HCOOH upon its 193 nm photolysis in an Ar matrix.⁵¹ The CO/CO₂ ratios for the channels shown in eqs 10 and 11 vary dramatically depending on the initial conformation. The 193 nm photolysis of *trans*-HCOOH predominantly follows channel shown in eq 11 with a CO/CO₂ ratio of 5.0, while the photolysis of *cis*-HCOOH, in contrast, gives a CO/CO₂ ratio of 0.42. These conformation-specific dynamics are termed “conformational memory”, and its mechanism has been clarified for the 1-iodopropane cation ($1\text{-C}_3\text{H}_7\text{I}^+$) and the propanal cation ($\text{C}_3\text{H}_6\text{O}^+$).⁵² However, a theoretical interpretation of the

mechanism of the conformational memory in HCOOH has not been very successful. We again performed SMF/ADDF and AMF/ADDF searches and identified the origin of the conformational memory.

Figure 6 shows the potential energy profiles (in kJ/mol) for the three states S_0 , S_1 , and T_1 of HCOOH obtained using MS-CASPT2 for S_0 and S_1 and SS-CASPT2 for T_1 with the (10e, 8o) active space and the aug-cc-pVDZ basis set.¹⁹ To compare the energetics with experimental thresholds, more reliable energies were calculated for selected important structures at the MS-(12e, 10o)-MRCISD(Q)/aug-cc-pVTZ//MS-(10e, 8o)-CASPT2/aug-cc-pVDZ and UCCSD(T)/aug-cc-pVTZ//UCCSD/aug-cc-pVTZ levels with the inclusion of zero-point vibrational energy corrections at the MS-(10e, 8o)-CASPT2/aug-cc-pVDZ level. These energy values are also shown in Figure 6 in parentheses and square brackets, respectively. In this application,¹⁹ 74 stationary structures were located. This large structural database includes pathways to higher-energy species such as dihydroxycarbene ($\text{HO}-\text{C}-\text{OH}$) and peroxy species, and some of them were found to be accessible with high photon energy. However, the channels that pass these species should be minor from an energetic viewpoint. Thus, for clarity, Figure 6 omits pathways that involve these high-energy species.

First, the experimental thresholds reported to date are interpreted using Figure 6. The origin band of the S_0 – S_1 transition of *trans*-HCOOH was observed at ~ 267 nm (448 kJ/mol), and our calculated energy value of 442.0 kJ/mol for 74 is reasonably similar. The molecule is fluorescent at lower than ~ 259 nm (462 kJ/mol), and a rapid decrease in fluorescence was observed at ~ 259 nm, which suggests the opening of a dissociation channel at this wavelength.^{50e,f} A similar threshold was found in a fluorescence quenching study.^{50g} However, no

clear explanation was available for this 259 nm threshold. Our interpretation, based in Figure 6, is that this threshold is related to MESX 72. From the S_1 minimum of 74, there is no accessible stationary point at lower than 462 kJ/mol except for 75 and 76 for the trans/cis isomerization. It is thus expected that the S_1/T_1 ISC occurs from 74 to 66 and from 75 to 67 with a trickling mechanism (without going through crossing), as is the case for formaldehyde. The S_1 PES is very close to the T_1 PES in the basin of HCOOH, and long residence allows slow S_1/T_1 ISC to take place inside the HCOOH basins. After the S_1/T_1 ISC, MESX 72 is the lowest gateway that escapes from the T_1 minima 66 and 67. Moreover, the calculated energy value of 462.2 kJ/mol for 72 is very close to the experimental threshold. After the S_0/T_1 ISC through MESX 72, the system predominantly undergoes molecular dissociations on S_0 to give CO + H₂O (via TS 57) and CO₂ + H₂ (via TS 59) because of their low barriers.

The experimental quantum yield of the HCO + OH channel (eq 13) is virtually zero below 475 kJ/mol (252 nm), and it gains intensity with an increase in the excitation energy.^{50e,f} This threshold is reproduced well by T_1 TS 69. Figure 6 shows that the other OH dissociation channel opens at 498.6 kJ/mol on the S_1 PES through S_1 TS 77. Because the ISC is a slow process, the direct OH dissociation on the S_1 PES will be dominant if the available excess energy is sufficient to overcome barrier 77 on the S_1 PES. The OH dissociation channel was observed to be dominant at 222 nm (539 kJ/mol) with an OH product quantum yield of ~0.80.^{50d} This is consistent with the experimental observation wherein different OH generation dynamics were observed for excitation energies of 244 nm (490.3 kJ/mol) and 230 nm (520.1 kJ/mol).^{50r} MECI 78 is present for the partially dissociated HCO····OH geometry. This MECI is close to the roaming pathway through TS 62 on the S_0 PES. After the nonadiabatic transition, CO + H₂O may be produced via the roaming OH dynamics.

The COOH + H generation channel (eq 12) opens at 472.4 kJ/mol via T_1 TS 71. A similar dissociation channel from the S_1 PES requires much higher excess energy (not shown in Figure 6 for clarity). This is consistent with a hydrogen (Rydberg) atom photofragment translational spectroscopy study, which showed that this channel occurs exclusively on the T_1 PES.⁵⁰ⁱ In this experiment, it was also found that the HCOO + H channel (eq 14) is on the S_1 PES, and the required energy was estimated to be ~532 kJ/mol.⁵⁰ⁱ As shown in Figure 6, this channel opens through S_1 TS 80. The barrier at 541.4 kJ/mol is in qualitative agreement with the experimental estimate of ~532 kJ/mol. A similar dissociation channel from the T_1 PES needs higher excess energy (not shown in Figure 6 for clarity), which is consistent with the experimental result. After dissociation through TS 80 and the subsequent nonadiabatic transition through MECI 81 at the partially dissociated HCOO····H geometry, the roaming dynamics for the generation of the molecular products CO₂ + H₂ may occur through S_0 TS 65.

In summary, on the basis of our calculation results, all of the low-photon-energy photodissociation channels of *trans*-HCOOH observed to date and their mechanisms can be explained as follows. Between 462 and 472 kJ/mol, two successive ISCs from S_1 to S_0 via T_1 followed by the molecular channels shown in eqs 10 and 11 on the S_0 PES are dominant. At 472 kJ/mol, a C–H bond dissociation channel (eq 12) opens on the T_1 PES. At 475 kJ/mol, an OH dissociation channel (eq 13) from the T_1 PES becomes accessible. Above

499 kJ/mol, a direct OH dissociation channel (eq 13) on the S_1 PES becomes dominant. Above 541 kJ/mol, a direct O–H bond dissociation channel (eq 14) becomes available on the S_1 PES. Overall, these results that were obtained by a systematic exploration of stationary structures are consistent with all of the experimental data. This result is highly encouraging for the future use of our photochemical GRRM strategy in combination with a proper quantum-chemical calculation method and kinetic theory for the prediction of elemental reaction channels for use in atmospheric modeling.

The remaining question is that of the conformational memory observed upon the 193 nm (620 kJ/mol) photolysis of *cis*-HCOOH. Figure 7 shows potential energy profiles that

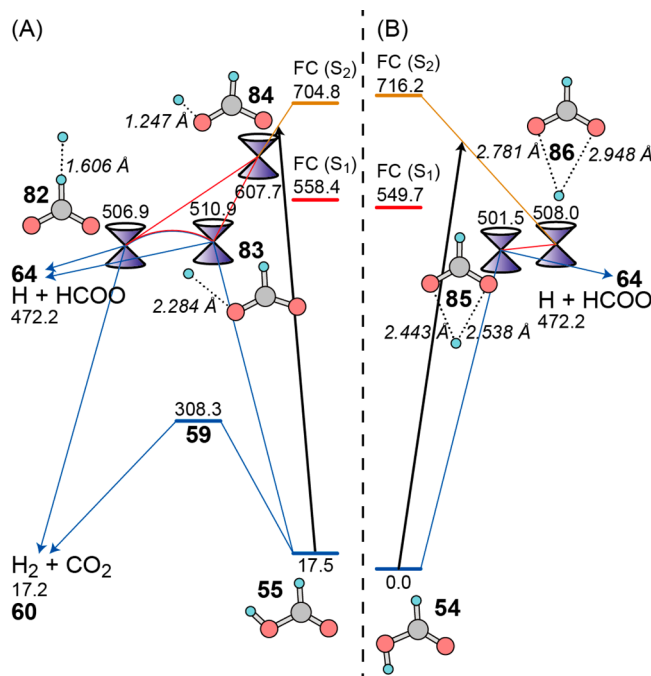


Figure 7. Potential energy profiles (in kJ/mol) for the three states S_0 (blue), S_1 (red), and S_2 (orange) of HCOOH. Cone marks represent the MECI points between the two singlet states. (A) Profiles for the conformation-specific dynamics starting from the FC point of *cis*-HCOOH. (B) Profiles for the conformation-specific dynamics starting from the FC point of *trans*-HCOOH.

provide a possible answer to this question. The S_{0-3} -MS-CASPT2/aug-cc-pVDZ was applied to the S_2/S_1 MECIs 84 and 86; S_{0-2} -MS-CASPT2/aug-cc-pVDZ to the S_1/S_0 MECIs 82, 83, and 85 and to the S_2 energy at the FC point; and S_{0-1} -MS-CASPT2/aug-cc-pVDZ to the other structures, all with a (10e, 8o) active space. During this photolysis, a total energy of 637.5 kJ/mol relative to *trans*-HCOOH is available. The photolysis was postulated to occur starting from the S_1 PES. Searches for the stationary structures as well as molecular dynamics simulations have been performed on the S_1 PES.^{50n-p} However, it is obvious from Figure 6 that isomerization from the *cis* isomer to the *trans* isomer occurs rapidly on the S_1 PES through a very low barrier of only 2.0 kJ/mol. In molecular dynamics simulations, this isomerization was found to occur immediately after photoexcitation. Thus, explanations of the conformation-specific dynamics for *cis*-HCOOH have not been successful in previous theoretical studies.

We found the S_0/S_1 MECIs 82 and 83 in the weakly interacting HCOO····H region with the partially dissociated H

atom in the *cis* conformation with respect to HCOO. After the nonadiabatic transition at MECI 82, the system settles to the S_0 PES, and barrierless H atom abstraction from the HCOO part by the partially dissociated H atom in the HCOO \cdots H complex occurs. This results in the generation of the molecular products $\text{CO}_2 + \text{H}_2$. Through MECI 83, a barrierless recombination between HCOO and H gives vibrationally highly excited *cis*-HCOOH. After the recombination, the excess energy localized in the O–H bond vibrational mode is expected to prefer, although not exclusively, a molecular dissociation to $\text{CO}_2 + \text{H}_2$ via TS 59 over dissociation to $\text{H}_2\text{O} + \text{CO}$ via TS 57. A question arises about how the partially dissociated HCOO \cdots H complex is generated on the S_1 PES, which is of substantially lower energy than the FC S_1 state.

The extensive structure list obtained by the automated search did not show any H atom dissociation pathway from the OH part of the S_1 minimum of 75. Instead, we found a cusp between the *cis* minimum 75 and the HCOO \cdots H region along a maximal ADD path, and this was calculated as an *approximate* path by the ADDF method. The cusp was found to be related to the S_1/S_2 conical intersection, where S_2 is an $n \rightarrow \sigma^*$ state. Starting from the cusp geometry, S_1/S_2 MECI 84 was obtained. Furthermore, geometry optimization at the MS-CASPT2 level on the S_2 PES starting from the FC geometry increased the O–H distance, and finally the S_1/S_2 MECI region was reached without a barrier. In other words, because of the $n \rightarrow \sigma^*$ repulsive character of S_2 , the H atom can dissociate on S_2 without a barrier through MECI 84 and then through S_1/S_0 MECIs 82 and 83. Importantly, S_1/S_2 MECI 84 and the S_1/S_0 MECIs 82 and 83 that led, without barrier, to the $\text{H}_2 + \text{CO}_2$ products contain the partially dissociated H in the *cis* conformation with respect to the HCOO hydrogen, and the two H atoms in the *cis* position can form a bond to dissociate as $\text{CO}_2 + \text{H}_2$.

The 193 nm ($620 + 17.5$ kJ/mol) photon energy is not enough to reach the S_2 PES at the FC geometry. Nevertheless, a fraction of the molecules can reach the S_2 PES with this photon energy at geometries slightly deviated from the FC point. Furthermore, the oscillator strength of 0.0362 for the $S_0 \rightarrow S_2$ transition at the FC point is much larger than the oscillator strength of 0.0009 for the $S_0 \rightarrow S_1$ transition at the MS-CAS(10e, 8o)-PT2/aug-cc-pVDZ level for the four lowest singlet states.

A similar path for *trans*-HCOOH also leads to H atom dissociation on the S_2 PES and two successive nonadiabatic transitions through S_1/S_2 MECI 86 and S_0/S_1 MECI 85. This results in the $\text{H} + \text{HCOO}$ products as well as the regeneration of the S_0 minimum 54 to maintain the *trans* conformation. In the *trans* conformation, the two hydrogen atoms are too distant to form the $\text{H}_2 + \text{CO}$ products. The S_2 path for *trans*-HCOOH is expected to be less important compared with *cis*-HCOOH because the excitation energy from S_0 to S_2 at the FC point for *trans*-HCOOH is substantially larger than that for the *cis* isomer.

Finally, our mechanism that involves rapid O–H bond dissociation on the S_2 PES is consistent with the other two cases that have been observed for $1\text{-C}_3\text{H}_7\text{I}^+$ and $\text{C}_3\text{H}_6\text{O}^+$ and involve an ultrafast descending process on the excited-state PES.⁵² In the actual experiment,⁵¹ the complete dissociation of the H atom on the S_1 PES can be prevented by an Ar matrix. Thus, QM/MM simulations considering the effects of surrounding Ar atoms explicitly by MM force fields^{53,54} are encouraged for a further understanding of the dynamics. We

also suggest that pathways starting from the S_1 PES are also in competition. If it is assumed that the S_1 path equally gives CO and CO_2 and also that the S_2 path produces only CO_2 , the observed CO/ CO_2 ratio of 0.42 can be explained by the contributions of 59% from the S_1 path and 41% from the S_2 path. We thus suggest that the CO/ CO_2 ratio can be further decreased by pumping the molecule exclusively to the S_2 PES. To obtain detailed statistics, further molecular dynamics simulations are encouraged.

Other Photodissociation Reactions. We have also reported many applications to other photodissociation reactions. Here these applications are summarized briefly. Two ketones, acetone and methyl ethyl ketone (MEK) were studied by the SMF and AMF approaches in combination with the double-ended ADDF method, assuming reaction products and intermediates. In the acetone study,^{20a} we proposed a slow intersystem crossing mechanism from S_1 to T_1 with a trickling mechanism similar to that of formaldehyde, followed by CH_3 dissociation via a TS on T_1 . This was found to be consistent with the observed long lifetime of the S_1 species of acetone. For MEK,^{20b} we discovered an unusual S_1/S_0 diradical mechanism involving H atom transfer on the S_1 surface followed by a nonadiabatic transition for a diradical isomer $\text{CH}_3\text{-C}(\cdot\text{OH})\text{-CH}_2\text{-CH}_2\cdot$. This mechanism was consistent with experimental photodissociation quantum yield measurements. Ketene is another example of a carbonyl compound.^{20d} In this reaction, using the SMF/ADDF and AMF/ADDF approaches, we located five nonadiabatic pathways starting from the S_2 FC point and using the six lowest PESs, $S_0\text{-}S_2$ and $T_1\text{-}T_3$, and we explained the five dissociation channels that were observed upon 193–215 nm photolysis.

For nitrogen-atom-containing systems, we studied the photolysis of methylamine and nitromethane and the collision reaction $\text{N}(^2\text{D}) + \text{H}_2\text{O}$. In these three studies, the SMF/ADDF and AMF/ADDF approaches were used. In a methylamine study,^{20f} in addition to all of the observed dissociation channels, the roaming channel involving the T_1 PES, which was recently suggested by an experimental group, was studied systematically. In the photolysis of nitromethane, a roaming isomerization reaction, i.e., $\text{CH}_3\text{NO}_2 \rightarrow \text{CH}_3\cdots\text{NO}_2 \rightarrow \text{CH}_3\text{ONO}$, was suggested and confirmed theoretically and experimentally. Our search also confirmed this channel, and in addition, other roaming channels were also predicted.^{20g} In the collision reaction $\text{N}(^2\text{D}) + \text{H}_2\text{O}$, the involvement of the D_1 PES was studied, but it was found that the channels that go through the D_1 PES are all minor.^{20h} For the D_0 PES, some roaming channels were predicted.

We also conducted SMF/MC-AFIR and AMF/MC-AFIR studies of combustion and photoaddition reactions. For the reactions between molecular oxygen and unsaturated hydrocarbon molecules, we found nonadiabatic channels that convert oxygen molecules from triplet to singlet on sp^2 carbon atoms.^{20c} For the photoaddition reaction between formaldehyde and ethylene molecules,^{20e} a comprehensive view of the reaction path network was obtained by SMF/MC-AFIR and AMF/MC-AFIR searches. Furthermore, the newly found S_1/T_1 MESX points suggested a significant contribution of S_1/T_1 ISC after C–O bond generation in the reaction intermediate, which was not considered in previous studies.

■ CONCLUSIONS AND PERSPECTIVES

In this Perspective, our approach toward the systematic exploration of photochemical reaction pathways has been

discussed. The SMF approach allows a systematic search for MESX and MECI structures in combination with local-minimum sampling methods that have been applied to the ground-state PES.¹⁵ With the AMF approach, the automated exploration of local-minimum and TS structures on the excited electronic state PESs can be performed using the automated reaction path search methods developed for the ground-state PES.¹⁶ Furthermore, the BPU method allows the accurate determination of MECI points without DCV calculations.¹⁷ These approaches have realized the automated exploration of photoreaction pathways.^{18–20}

In our studies, the ADDF method was used for initial structure exploration.¹² In this step, CASSCF or CASPT2 with a small active space and basis set was adopted to reduce the computational cost. The topography of the excited-state PESs may change significantly depending on the choice of theoretical level. Therefore, the pathways obtained by the initial automatic search at a low theoretical level have to be confirmed using a higher-level theoretical method. This procedure has been most difficult and still requires sufficient knowledge about the excited-state chemistry. Nevertheless, the initial automatic and unbiased search provides many useful hints that would not be available otherwise and has led to the discovery of unexpected reaction mechanisms, as demonstrated and discussed above.

The above-mentioned results are highly encouraging for the theoretical prediction of elementary reaction channels for atmospheric modeling. Many unknown features of photodissociation reactions have been found for several important photochemical reactions by the use of the GRRM strategy. We plan to use the present strategy and code for future challenges in this and related areas.

We again emphasize that the present approach is useful for a qualitative understanding of reaction mechanism overviews. For roaming pathways, quantitative discussions are difficult when only traditional TST-like simulations based only on local-minimum and saddle-point geometries are considered.⁷ For the quantitative prediction of branching ratios, reaction time scales, and product energy distributions, among others, molecular dynamics simulations that account for the coupling of adiabatic potentials are recommended.

Our interest has recently been expanded to the study and design of photofunctional molecules for applications such as bioimaging, photoswitching, and photosensitizers using the GRRM strategy. The structures and energies of the MECIs and MESXs determine the efficiency of nonadiabatic transitions that are closely related to the functionality of these molecules. In complex photofunctional molecules, many MECIs and MESXs are expected to exist for various distorted structures. The presented unbiased and untargeted search will allow the identification of the kinds of molecular distortions that cause crossing and thus quenching, such as rotation around double bonds and out-of-plane distortions of conjugated structures. This theoretical information is difficult to obtain otherwise, and opportunities are thus provided to control and design more efficient photofunctional molecules.

For this purpose, we have combined the SMF approach with TDDFT.⁵⁵ One of the most serious drawbacks of TDDFT is that it cannot describe the conical intersection between the reference ground state and the first excited state with the same spin and space symmetry.⁵⁶ This problem has been eliminated by spin-flip TDDFT (SF-TDDFT).⁵⁷ SF-TDDFT can be used for the optimization of the geometries of MECIs between these states.⁵⁸ We have thus developed an efficient, automated MECI

explorer by combining the SMF approach, SF-TDDFT, and SC-AFIR.⁵⁹ This combined approach is currently being used in practical applications such as the analysis and design of photofunctional molecules containing 30–50 atoms.

■ ASSOCIATED CONTENT

§ Supporting Information

Full citations for refs 25 and 26. This material is available free of charge via the Internet at <http://pubs.acs.org>.

■ AUTHOR INFORMATION

Corresponding Authors

*smaeda@mail.sci.hokudai.ac.jp

*morokuma@fukui.kyoto-u.ac.jp

Notes

The authors declare no competing financial interest.

■ ACKNOWLEDGMENTS

This work was partly supported by the Japan Science and Technology Agency (JST) through a Core Research for Evolutional Science and Technology (CREST) grant in the area of High Performance Computing for Multiscale and Multiphysics Phenomena at Kyoto University and a CREST grant in the area of Establishment of Molecular Technology towards the Creation of New Functions at Hokkaido University; the U.S. AFOSR (Grant FA9550-10-1-0304) at Emory University; and the Japan Society for the Promotion of Science (JSPS) through a Grant-in-Aid for Scientific Research (A) (24245005) at Kyoto University and a Grant-in-Aid for Young Researchers (A) (23685004) at Hokkaido University. We also deeply thank our collaborators, Prof. Simon W. North and Dr. Michael P. Grubb of Texas A&M University; Prof. Joel M. Bowman and Dr. Bina Fu of Emory University; Prof. Sándor Dóbbé, Dr. Rebeka Nádasdi, Dr. Gábor L. Zügner, and Dr. Mária Farkas of the Chemical Research Center of the Hungarian Academy of Sciences; Dr. Hongyan Xiao, Dr. Fengyi Liu, Dr. Miho Isegawa, and Dr. Noriyuki Minezawa of Kyoto University; and Dr. Yu Harabuchi of Hokkaido University.

■ REFERENCES

- (1) (a) Hehre, W. J.; Radom, L.; Pople, J. A.; Schleyer, P. v. R. *Ab Initio Molecular Orbital Theory*; Wiley: New York, 1986. (b) Parr, R. G.; Yang, W. *Density-Functional Theory of Atoms and Molecules*; Oxford University Press: New York, 1989. (c) Jensen, F. *Introduction to Computational Chemistry*, 2nd ed.; Wiley: Chichester, U.K., 2007.
- (2) (a) Fernández-Ramos, A.; Miller, J. A.; Klippenstein, S. J.; Truhlar, D. G. *Chem. Rev.* **2006**, *106*, 4518–4584. (b) Klippenstein, S. J.; Pande, V. S.; Truhlar, D. G. *J. Am. Chem. Soc.* **2014**, *136*, 528–546 and references therein.
- (3) Vereecken, L.; Francisco, J. S. *Chem. Soc. Rev.* **2012**, *41*, 6259–6293 and references therein.
- (4) For example, see: (a) Gelbart, W. N. *Annu. Rev. Phys. Chem.* **1977**, *28*, 323–348. (b) Simons, J. P. *J. Phys. Chem.* **1984**, *88*, 1287–1293. (c) Butler, L. J.; Neumark, D. M. *J. Phys. Chem.* **1996**, *100*, 12801–12816. (d) Sato, H. *Chem. Rev.* **2001**, *101*, 2687–2725. (e) Moore, C. B. *Annu. Rev. Phys. Chem.* **2007**, *58*, 1–33 and references therein.
- (5) van Zee, R. D.; Foltz, M. F.; Moore, C. B. *J. Chem. Phys.* **1993**, *99*, 1664–1673.
- (6) Townsend, D.; Lahankar, S. A.; Lee, S. K.; Chambreaux, S. D.; Suits, A. G.; Zhang, X.; Rheinecker, J.; Harding, L. B.; Bowman, J. M. *Science* **2004**, *306*, 1158–1161.
- (7) (a) Suits, A. G. *Acc. Chem. Res.* **2008**, *41*, 873–881. (b) Bowman, J. M.; Shepler, B. C. *Annu. Rev. Phys. Chem.* **2011**, *62*, 531–553.

- (c) Herath, N.; Suits, A. G. *J. Phys. Chem. Lett.* **2011**, *2*, 642–647.
(d) Bowman, J. M.; Suits, A. G. *Phys. Today* **2011**, *64*, 33–37.
(e) Bowman, J. M. *Mol. Phys.* **2014**, *112*, 2516–2528.
(8) (a) Yarkony, D. R. *Rev. Mod. Phys.* **1996**, *68*, 985–1013.
(b) Bernardi, F.; Olivucci, M.; Robb, M. A. *Chem. Soc. Rev.* **1996**, *25*, 321–328. (c) Sobolewski, A. L.; Domcke, W.; Dedonder-Lardeux, C.; Jouvet, C. *Phys. Chem. Chem. Phys.* **2002**, *4*, 1093–1100. (d) Levine, B. G.; Martinez, T. J. *Annu. Rev. Phys. Chem.* **2007**, *58*, 613–634.
(e) Nanbu, S.; Ishida, T.; Nakamura, H. *Chem. Sci.* **2010**, *1*, 663–674.
(9) (a) Schlegel, H. B. *J. Comput. Chem.* **2003**, *24*, 1514–1527.
(b) Schlegel, H. B. *Wiley Interdiscip. Rev.: Comput. Mol. Sci.* **2011**, *1*, 790–809 and references therein.
(10) (a) Koga, N.; Morokuma, K. *Chem. Phys. Lett.* **1985**, *119*, 371–374. (b) Manaa, M. R.; Yarkony, D. R. *J. Chem. Phys.* **1993**, *99*, 5251–5256. (c) Bearpark, M. J.; Robb, M. A.; Schlegel, H. B. *Chem. Phys. Lett.* **1994**, *223*, 269–274. (d) Anglada, J. M.; Bofill, J. M. *J. Comput. Chem.* **1997**, *18*, 992–1003. (e) Ciminelli, C.; Granucci, G.; Persico, M. *Chem.—Eur. J.* **2004**, *10*, 2327–2341. (f) Keal, T. W.; Koslowski, A.; Thiel, W. *Theor. Chem. Acc.* **2007**, *118*, 837–844. (g) Levine, B. G.; Coe, J. D.; Martinez, T. J. *J. Phys. Chem. B* **2008**, *112*, 405–413. (h) Sicilia, F.; Blancafort, L.; Bearpark, M. J.; Robb, M. A. *J. Chem. Theory Comput.* **2008**, *4*, 257–266.
(11) For example, see: (a) Jasper, A. W.; Nangia, S.; Zhu, C.; Truhlar, D. G. *Acc. Chem. Res.* **2006**, *39*, 101–108. (b) Martinez, T. J. *Acc. Chem. Res.* **2006**, *39*, 119–126. (c) Lasorne, B.; Worth, G. A.; Robb, M. A. *Wiley Interdiscip. Rev.: Comput. Mol. Sci.* **2011**, *1*, 460–475. (d) Barbatti, M. *Wiley Interdiscip. Rev.: Comput. Mol. Sci.* **2011**, *1*, 620–633. (e) Curchod, B. F. E.; Rothlisberger, U.; Tavernelli, I. *ChemPhysChem* **2013**, *14*, 1314–1340 and references therein.
(12) (a) Ohno, K.; Maeda, S. *Chem. Phys. Lett.* **2004**, *384*, 277–282. (b) Maeda, S.; Ohno, K. *J. Phys. Chem. A* **2005**, *109*, 5742–5753. (c) Ohno, K.; Maeda, S. *J. Phys. Chem. A* **2006**, *110*, 8933–8941. (d) Maeda, S.; Taketsugu, T.; Morokuma, K.; Ohno, K. *Bull. Chem. Soc. Jpn.* **2014**, *87*, 1315–1334.
(13) (a) Maeda, S.; Morokuma, K. *J. Chem. Phys.* **2010**, *132*, No. 241102. (b) Maeda, S.; Komagawa, S.; Uchiyama, M.; Morokuma, K. *Angew. Chem., Int. Ed.* **2011**, *50*, 644–649. (c) Maeda, S.; Morokuma, K. *J. Chem. Theory Comput.* **2011**, *7*, 2335–2345. (d) Maeda, S.; Taketsugu, T.; Morokuma, K. *J. Comput. Chem.* **2014**, *35*, 166–173.
(14) Maeda, S.; Ohno, K.; Morokuma, K. *Phys. Chem. Chem. Phys.* **2013**, *15*, 3683–3701.
(15) Maeda, S.; Ohno, K.; Morokuma, K. *J. Phys. Chem. A* **2009**, *113*, 1704–1710.
(16) Maeda, S.; Ohno, K.; Morokuma, K. *Adv. Phys. Chem.* **2012**, No. 268124.
(17) Maeda, S.; Ohno, K.; Morokuma, K. *J. Chem. Theory Comput.* **2010**, *6*, 1538–1545.
(18) Xiao, H.-Y.; Maeda, S.; Morokuma, K. *J. Phys. Chem. Lett.* **2011**, *2*, 934–938.
(19) Maeda, S.; Taketsugu, T.; Morokuma, K. *J. Phys. Chem. Lett.* **2012**, *3*, 1900–1907.
(20) (a) Maeda, S.; Ohno, K.; Morokuma, K. *J. Phys. Chem. Lett.* **2010**, *1*, 1841–1845. (b) Nádasdi, R.; Zügner, G. L.; Farkas, M.; Dóbbé, S.; Maeda, S.; Morokuma, K. *ChemPhysChem* **2010**, *11*, 3883–3895. (c) Maeda, S.; Saito, R.; Morokuma, K. *J. Phys. Chem. Lett.* **2011**, *2*, 852–857. (d) Xiao, H.-Y.; Maeda, S.; Morokuma, K. *J. Phys. Chem. A* **2013**, *117*, 7001–7008. (e) Maeda, S.; Taketsugu, T.; Morokuma, K. *Z. Phys. Chem.* **2013**, *227*, 1421–1433. (f) Xiao, H.-Y.; Maeda, S.; Morokuma, K. *J. Phys. Chem. A* **2013**, *117*, 5757–5764. (g) Isegawa, M.; Liu, F.; Maeda, S.; Morokuma, K. *J. Chem. Phys.* **2014**, *140*, No. 244310. (h) Isegawa, M.; Liu, F.; Maeda, S.; Morokuma, K. *J. Chem. Phys.* **2014**, *141*, No. 154303.
(21) Maeda, S.; Harabuchi, Y.; Osada, Y.; Taketsugu, T.; Morokuma, K.; Ohno, K. *GRRM14*; http://grrm.chem.tohoku.ac.jp/GRRM/index_e.html (accessed Dec 3, 2014).
(22) Banerjee, A.; Adams, N.; Simons, J.; Shepard, R. J. *J. Phys. Chem.* **1985**, *89*, 52–57.
(23) (a) Maeda, S.; Ohno, K. *Chem. Phys. Lett.* **2005**, *404*, 95–99. (b) Maeda, S.; Ohno, K. *J. Chem. Phys.* **2006**, *124*, No. 174306.
(24) Choi, C.; Elber, R. *J. Chem. Phys.* **1991**, *94*, 751–760.
(25) Werner, H.-J.; et al. *MOLPRO, A Package of Ab Initio Programs*, version 2012.1; <http://www.molpro.net> (accessed Dec 3, 2014).
(26) Frisch, M. J.; et al. *Gaussian 09*, revision D.01; Gaussian, Inc.: Wallingford, CT, 2009.
(27) Schmidt, M. W.; Baldridge, K. K.; Boatz, J. A.; Elbert, S. T.; Gordon, M. S.; Jensen, J. H.; Koseki, S.; Matsunaga, N.; Nguyen, K. A.; Su, S.-J.; Windus, T. L.; Dupuis, M.; Montgomery, J. A., Jr. *J. Comput. Chem.* **1993**, *14*, 1347–1363.
(28) (a) Gelbart, W. M.; Elert, M. L.; Heller, D. F. *Chem. Rev.* **1980**, *80*, 403–416. (b) Moore, C. B.; Weisshaar, J. C. *Annu. Rev. Phys. Chem.* **1983**, *34*, 525–555. (c) Clouthier, D. J.; Ramsay, D. A. *Annu. Rev. Phys. Chem.* **1983**, *34*, 31–58. (d) Green, W. H., Jr.; Moore, C. B.; Polik, W. F. *Annu. Rev. Phys. Chem.* **1992**, *43*, 591–626.
(29) (a) Hayes, D. M.; Morokuma, K. *Chem. Phys. Lett.* **1972**, *12*, 539–543. (b) Jaffe, R. L.; Hayes, D. M.; Morokuma, K. *J. Chem. Phys.* **1974**, *60*, 5108–5109. (c) Hernandez, J. A.; Carbo, R. *J. Chim. Phys.-Chim. Biol.* **1975**, *72*, 959–960. (d) Jaffe, R. L.; Morokuma, K. *J. Chem. Phys.* **1976**, *64*, 4881–4886. (e) Goddard, J. D.; Schaefer, H. F., III. *J. Chem. Phys.* **1979**, *70*, 5117–5134. (f) Handy, N. C.; Carter, S. *Chem. Phys. Lett.* **1981**, *79*, 118–124. (g) Schinke, R. *J. Chem. Phys.* **1986**, *84*, 1487–1491. (h) Scuseria, G. E.; Schaefer, H. F., III. *J. Chem. Phys.* **1989**, *90*, 3629–3636. (i) Davis, H. L.; Wales, D. J.; Berry, R. S. *J. Chem. Phys.* **1990**, *92*, 4308–4319. (j) Chang, Y. T.; Minichino, C.; Miller, W. H. *J. Chem. Phys.* **1992**, *96*, 4341–4355. (k) Deng, L.; Ziegler, T.; Fan, L. *J. Chem. Phys.* **1993**, *99*, 3823–3835. (l) Chen, W.; Hase, W. L.; Schlegel, H. B. *Chem. Phys. Lett.* **1994**, *228*, 436–442. (m) Peslherbe, G. H.; Hase, W. L. *J. Chem. Phys.* **1996**, *104*, 7882–7894. (n) Bondensgård, K.; Jensen, F. *J. Chem. Phys.* **1996**, *104*, 8025–8031. (o) Nakano, H.; Nakayama, K.; Hirao, K.; Dupuis, M. *J. Chem. Phys.* **1997**, *106*, 4912–4917. (p) Quapp, W.; Hirsch, M.; Imig, O.; Heidrich, D. *J. Comput. Chem.* **1998**, *19*, 1087–1100. (q) Jensen, F. *Theor. Chem. Acc.* **1998**, *99*, 295–300. (r) Feller, D.; Dupuis, M.; Garrett, B. C. *J. Chem. Phys.* **2000**, *113*, 218–226. (s) Li, X.; Millam, J. M.; Schlegel, H. B. *J. Chem. Phys.* **2000**, *113*, 10062–10067. (t) Schlegel, H. B.; Iyengar, S. S.; Li, X.; Millam, J. M.; Voth, G. A.; Scuseria, G. E.; Frisch, M. J. *J. Chem. Phys.* **2002**, *117*, 8694–8704. (u) Yonehara, T.; Kato, S. *J. Chem. Phys.* **2003**, *117*, 11131–11138. (v) Zhang, X.; Zou, S.; Harding, L. B.; Bowman, J. M. *J. Phys. Chem. A* **2004**, *108*, 8980–8986. (w) Yonehara, T.; Kato, S. *J. Chem. Phys.* **2006**, *125*, No. 084307.
(30) (a) Yamaguchi, Y.; Wesolowski, S. S.; van Huis, T. J.; Schaefer, H. F., III. *J. Chem. Phys.* **1998**, *108*, 5281–5288. (b) Yin, H. M.; Kable, S. H.; Zhang, X.; Bowman, J. M. *Science* **2006**, *311*, 1443–1446.
(31) (a) Baek, K. K. *J. Chem. Phys.* **2000**, *112*, 1–4. (b) Simonsen, J. B.; Rusteika, N.; Johnson, M. S.; Sølling, T. I. *Phys. Chem. Chem. Phys.* **2008**, *10*, 674–680.
(32) Shepler, B. C.; Epifanovsky, E.; Zhang, P.; Bowman, J. M.; Krylov, A. I.; Morokuma, K. *J. Phys. Chem. A* **2008**, *112*, 13267–13270.
(33) Zhang, P.; Maeda, S.; Morokuma, K.; Braams, B. J. *J. Chem. Phys.* **2009**, *130*, No. 114304.
(34) Fu, B.; Shepler, B. C.; Bowman, J. M. *J. Am. Chem. Soc.* **2011**, *133*, 7957–7968.
(35) Araujo, M.; Lasorne, B.; Bearpark, M. J.; Robb, M. A. *J. Phys. Chem. A* **2008**, *112*, 7489–7491.
(36) (a) Araújo, M.; Lasorne, B.; Magalhães, A. L.; Worth, G. A.; Bearpark, M. J.; Robb, M. A. *J. Chem. Phys.* **2009**, *131*, No. 144301. (b) Araújo, M.; Lasorne, B.; Magalhães, A. L.; Bearpark, M. J.; Robb, M. A. *J. Phys. Chem. A* **2010**, *114*, 12016–12020.
(37) Harding, L. B.; Klippenstein, S. J.; Jasper, A. W. *Phys. Chem. Chem. Phys.* **2007**, *9*, 4055–4070.
(38) Maeda, S.; Ohno, K. *Chem. Phys. Lett.* **2008**, *460*, 55–58.
(39) Shepler, B. C.; Han, Y.-C.; Bowman, J. M. *J. Phys. Chem. Lett.* **2011**, *2*, 834–838.
(40) For example, see: (a) Zhu, R. S.; Lin, M. C. *Chem. Phys. Lett.* **2009**, *478*, 11–16. (b) Harding, L. B.; Klippenstein, S. J. *J. Phys. Chem. Lett.* **2010**, *1*, 3016–3020. (c) Hause, M. L.; Herath, N.; Zhu, R.; Lin,

- M. C.; Suits, A. G. *Nat. Chem.* **2011**, *3*, 932–937. (d) Zhu, R. S.; Raghunath, P.; Lin, M. C. *J. Phys. Chem. A* **2013**, *117*, 7308–7313.
- (41) For example, see: (a) Zhang, X.; Rheinecker, J. L.; Bowman, J. M. *J. Chem. Phys.* **2005**, *122*, No. 114313. (b) Bowman, J. M.; Zhang, X. *Phys. Chem. Chem. Phys.* **2006**, *8*, 321–332. (c) Heazlewood, B. R.; Jordan, M. J. T.; Kable, S. H.; Selby, T. M.; Osborn, D. L.; Shepler, B. C.; Braams, B. J.; Bowman, J. M. *Proc. Natl. Acad. Sci. U.S.A.* **2008**, *105*, 12719–12724. (d) Shepler, B. C.; Braams, B. J.; Bowman, J. M. *J. Phys. Chem. A* **2008**, *112*, 9344–9351. (e) Han, Y.-C.; Shepler, B. C.; Bowman, J. M. *J. Phys. Chem. Lett.* **2011**, *2*, 1715–1719. (f) Fu, B.; Han, Y.-C.; Bowman, J. M. *Faraday Discuss.* **2012**, *157*, 27–39. (g) Homayoon, Z.; Bowman, J. M. *J. Phys. Chem. A* **2013**, *117*, 11665–11672.
- (42) Klippenstein, S. J.; Georgievskii, Y.; Harding, L. B. *J. Phys. Chem. A* **2011**, *115*, 14370–14381.
- (43) Andrews, D. U.; Kable, S. H.; Jordan, M. J. T. *J. Phys. Chem. A* **2013**, *117*, 7631–7642.
- (44) (a) Magnotta, F.; Johnston, H. S. *Geophys. Res. Lett.* **1980**, *7*, 769–772. (b) Davis, H. F.; Kim, B.; Johnston, H. S.; Lee, Y. T. *J. Phys. Chem.* **1993**, *97*, 2172–2180. (c) Orlando, J. J.; Tyndall, G. S.; Moortgat, G. K.; Calvert, J. G. *J. Phys. Chem.* **1993**, *97*, 10996–11000. (d) Mikhaylichenko, K.; Riehn, C.; Valachovic, L.; Sanov, A.; Wittig, C. *J. Chem. Phys.* **1996**, *105*, 6807–6817. (e) Eisfeld, W.; Morokuma, K. *J. Chem. Phys.* **2000**, *113*, 5587–5597. (f) Eisfeld, W.; Morokuma, K. *J. Chem. Phys.* **2001**, *114*, 9430–9440. (g) Eisfeld, W.; Morokuma, K. *J. Chem. Phys.* **2003**, *119*, 4682–4688. (h) Okumura, M.; Stanton, J. F.; Deev, A.; Sommar, J. *Phys. Scr.* **2006**, *73*, C64–C70.
- (45) (a) Grubb, M. P.; Warter, M. L.; Suits, A. G.; North, S. W. *J. Phys. Chem. Lett.* **2010**, *1*, 2455–2458. (b) Grubb, M. P.; Warter, M. L.; Kurt, M. J.; North, S. W. *J. Phys. Chem. A* **2011**, *115*, 3218–3226.
- (46) (a) Grubb, M. P.; Warter, M. L.; Xiao, H.-Y.; Maeda, S.; Morokuma, K.; North, S. W. *Science* **2012**, *335*, 1075–1078. (b) Grubb, M. P.; Warter, M. L.; North, S. W. *Phys. Chem. Chem. Phys.* **2012**, *14*, 6733–6740.
- (47) Xiao, H.-Y.; Maeda, S.; Morokuma, K. *J. Chem. Theory Comput.* **2012**, *8*, 2600–2605.
- (48) Fu, B.; Bowman, J. M.; Xiao, H.-Y.; Maeda, S.; Morokuma, K. *J. Chem. Theory Comput.* **2013**, *9*, 2882–2886.
- (49) Fernando, R.; Dey, A.; Broderick, B. M.; Fu, B.; Homayoon, Z.; Bowman, J. M.; Suits, A. G. *J. Phys. Chem. A* **2015**, DOI: 10.1021/jp509902d.
- (50) (a) Jolly, G. S.; Singleton, D. L.; Paraskevopoulos, G. *J. Phys. Chem.* **1987**, *91*, 3463–3465. (b) Ebata, T.; Fujii, A.; Amano, T.; Ito, M. *J. Phys. Chem.* **1987**, *91*, 6095–6097. (c) Ebata, T.; Amano, T.; Ito, M. *J. Chem. Phys.* **1989**, *90*, 6095–6097. (d) Singleton, D. L.; Paraskevopoulos, G.; Irwin, R. S. *J. Phys. Chem.* **1990**, *94*, 695–699. (e) Brouard, M.; Simons, J. P.; Wang, J.-X. *Faraday Discuss. Chem. Soc.* **1991**, *91*, 63–72. (f) Brouard, M.; Wang, J.-X. *J. Chem. Soc., Faraday Trans.* **1992**, *88*, 3511–3516. (g) Abe, H.; Hayashi, H. *J. Phys. Chem.* **1994**, *98*, 2797–2802. (h) Lundell, J.; Räsänen, M. *J. Mol. Struct.* **1997**, *436–437*, 349–358. (i) Langford, S. R.; Batten, A. D.; Kono, M.; Ashfold, M. N. R. *J. Chem. Soc., Faraday Trans.* **1997**, *93*, 3757–3764. (j) Shin, S. K.; Han, E. J.; Kim, H. L. *J. Photochem. Photobiol., A* **1998**, *118*, 71–74. (k) Tabayashi, K.; Aoyama, J.; Matsui, M.; Hino, T.; Saito, K. *J. Chem. Phys.* **1999**, *110*, 9547–9554. (l) Su, H.; He, Y.; Kong, F.; Fang, W.; Liu, R. *J. Chem. Phys.* **2000**, *113*, 1891–1897. (m) Lee, K. W.; Lee, K.-S.; Jung, K.-H.; Volpp, H.-R. *J. Chem. Phys.* **2002**, *117*, 9266–9274. (n) He, H.-Y.; Fang, W.-H. *J. Am. Chem. Soc.* **2003**, *125*, 16139–16147. (o) Martínez-Núñez, E.; Vázquez, S. A.; Borges, I., Jr.; Rocha, A. B.; Estévez, C. M.; Castillo, J. F.; Aoiz, F. J. *J. Phys. Chem. A* **2005**, *109*, 2836–2839. (p) Martínez-Núñez, E.; Vázquez, S.; Granucci, G.; Persico, M.; Estevez, C. M. *Chem. Phys. Lett.* **2005**, *412*, 35–40. (q) Kurosaki, Y.; Yokoyama, K.; Teranishi, Y. *Chem. Phys.* **2005**, *308*, 325–334. (r) Huang, C.; Zhang, C.; Yang, X. *J. Chem. Phys.* **2010**, *132*, No. 154306.
- (51) Khriachtchev, L.; Macôas, E.; Pettersson, M.; Räsänen, M. *J. Am. Chem. Soc.* **2002**, *124*, 10994–10995.
- (52) (a) Park, S. T.; Kim, S. K.; Kim, M. S. *Nature* **2002**, *415*, 306–308. (b) Kim, M. H.; Shen, L.; Tao, H.; Martinez, T. J.; Suits, A. G. *Science* **2007**, *315*, 1561–1565. (c) Singh, P. C.; Shen, L.; Kim, M. H.; Suits, A. G. *Chem. Sci.* **2010**, *1*, 552–560. (d) Tao, H.; Shen, L.; Kim, M. H.; Suits, A. G.; Martinez, T. J. *J. Chem. Phys.* **2011**, *134*, No. 054313.
- (53) Eckert-Maksić, M.; Vazdar, M.; Ruckebauer, M.; Barbatti, M.; Müller, T.; Lischka, H. *Phys. Chem. Chem. Phys.* **2010**, *12*, 12719–12726.
- (54) Niimi, K.; Nakayama, A.; Ono, Y.; Taketsugu, T. *J. Phys. Chem. A* **2014**, *118*, 380–387.
- (55) Harabuchi, Y.; Maeda, S.; Taketsugu, T.; Minezawa, N.; Morokuma, K. *J. Chem. Theory Comput.* **2013**, *9*, 4116–4123.
- (56) Levine, B. G.; Ko, C.; Quenneville, J.; Martinez, T. J. *Mol. Phys.* **2006**, *104*, 1039–1051.
- (57) Shao, Y. H.; Head-Gordon, M.; Krylov, A. I. *J. Chem. Phys.* **2003**, *118*, 4807–4818.
- (58) Minezawa, N.; Gordon, M. S. *J. Phys. Chem. A* **2009**, *113*, 12749–12753.
- (59) Maeda, S.; Harabuchi, Y.; Taketsugu, T.; Morokuma, K. *J. Phys. Chem. A* **2014**, *118*, 12050–12058.